Dalton Transactions

PAPER

View Article Online
View Journal | View Issue

Cite this: *Dalton Trans.*, 2016, **45**, 324

Carbonic anhydrase mimics for enhanced CO_2 absorption in an amine-based capture solvent†

Rachael A. Kelsey,[a] David A. Miller,[a] Sean R. Parkin,[a] Kun Liu,[b] Joe E. Remias,[b] Yue Yang,[c] Felice C. Lightstone,[c] Kunlei Liu,[b,d] Cameron A. Lippert*[b] and Susan A. Odom*[a]

Received 30th July 2015,
Accepted 13th November 2015

DOI: 10.1039/c5dt02943k

www.rsc.org/dalton

Two new small-molecule enzyme mimics of carbonic anhydrase were prepared and characterized. These complexes contain the salen-like ligand bis(hydroxyphenyl)phenanthroline. This ligand is similar to the salen-type ligands previously incorporated into carbonic anhydrase mimics but contains no hydrolyzable imine groups and therefore serves as a promising ligand scaffold for the synthesis of a more robust CO_2 hydration catalyst. These homogeneous catalysts were investigated for CO_2 hydration in concentrated primary amine solutions through which a dilute CO_2 (14%) fluid stream was flowed and showed exceptional activity for increased CO_2 absorption rates.

Introduction

The emission of greenhouse gases such as carbon dioxide (CO_2) plays a central role in the increase of the Earth's surface temperature and ocean acidity, leading to irreversible, detrimental climate changes. The majority of anthropogenic CO_2 arises from industrial processes; the largest source is the combustion of fossil fuels for electricity, which produces billions of tons of CO_2 annually.[1] To reduce CO_2 emissions, in January 2014, the US EPA released new recommendations that all new coal-burning and natural gas-burning power plants in the USA have emissions limits of 1100 lb and 1000 lb CO_2 per MWh, respectively, of electricity generated.[2] These regulations will require partial implementation of carbon capture and storage for coal-fired power plants. In June 2014, the EPA released additional proposed regulations to limit CO_2 from existing electric utility-generating units toward a goal of cutting CO_2 emissions from the power sector by up to 30% by 2030, using 2005 emissions as a baseline.[3] Ethanolamine and other primary and secondary amines can be used to capture CO_2 through direct reaction with CO_2 or – in a slower reaction – with bicarbonate (HCO_3^-), the latter of which forms after CO_2 hydration.[4] Increasing the rate of CO_2 hydration in amine solvents could increase the mass transfer coefficients of a carbon-capture system, thereby significantly lowering capital costs for carbon-capture plant construction.

Carbon dioxide hydration occurs in nature in metalloproteins called carbonic anhydrases (CAs) with rate constants of up to 10^6 M^{-1} s^{-1} at ambient conditions and at physiological pH.[5] Despite its efficient reaction in nature, the frailty of these proteins prevents their industrial use in amine-based capture solvents, as they denature at elevated temperatures and are inhibited in the highly concentrated amine solutions (~30 wt %) employed in carbon capture, which are highly basic and corrosive (Fig. S1†).[6] While CAs are unsuitable for use in the concentrated, aqueous amine-based solvents used for carbon capture in power plants, they serve as candidates for the development of biomimetic catalysts for utilization in enhancing industrial carbon capture and are an inspiration in the design of enzyme mimics.

The development and study of CA mimics for CO_2 hydration has been explored by several research groups.[7] The majority of mimics studied are structural analogs of the enzyme's active site and have shown little to no activity toward CO_2 hydration. Direct structural mimics tend to dimerize, strongly bind anions, and perform undesirable side reactions due to the lack of a secondary coordination environment to control the reaction process. The generally accepted mechanism of CO_2 hydration by CA and its mimics involves the nucleophilic attack by a Zn-based hydroxyl group of a dissolved CO_2 mole-

[a]*Department of Chemistry, University of Kentucky, Lexington, KY 40506-0055, USA. E-mail: susan.odom@uky.edu*
[b]*Center for Applied Energy Research, University of Kentucky, Lexington, KY 40511-8410, USA. E-mail: cameron.lippert@uky.edu*
[c]*Division, Lawrence Livermore National Laboratory, Livermore, CA 94550-9234, USA. E-mail: lightstone1@llnl.gov*
[d]*Department of Mechanical Engineering, Biosciences and Biotechnology, University of Kentucky, Lexington, 40511-8410 KY, USA. E-mail: kunlei.liu@uky.edu*

†Electronic supplementary information (ESI) available: Breakthrough testing with carbonic anhydrase. CO_2 absorption studies with Zn–cyclen in 30% MEA. Schematic of pH-drop and solvent breakthrough testing apparatus. Important bond lengths, angles, and dihedrals of **1** and **2**. Structural overlays of computed complexes with crystal structures. Energy profile of the CO_2 addition step. Atomic coordinate. CCDC 1415828 and 1009783. For ESI and crystallographic data in CIF or other electronic format see DOI: 10.1039/c5dt02943k

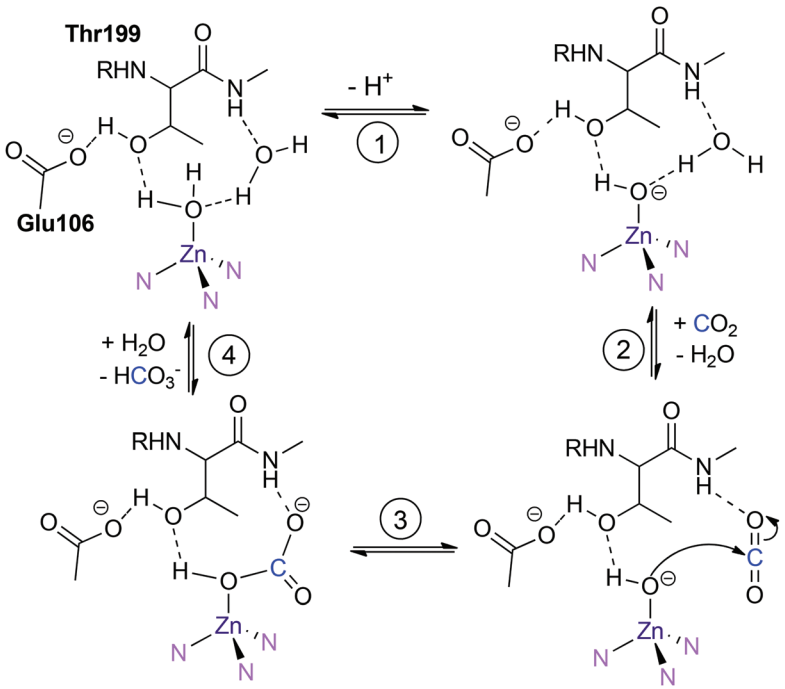

Scheme 1 Proposed mechanism of CA showing (1) deprotonation, (2) CO_2 activation, (3) bicarbonate formation, and (4) bicarbonate substitution with water in which N atoms come from histidine residues.

cule, which generates a molecule of bicarbonate (Scheme 1). Significant catalytic and mechanistic work has been performed on active-site mimics, including $[Zn^{II}(cyclen)(H_2O)][ClO_4]_2$, one of the most efficient mimics.[7a–c] However, we observed this complex to be inactive under conditions conducive to industrial carbon capture, *i.e.* low CO_2 (0.14 atm) and high primary amine concentrations (5 M) (Fig. S2†). We also observed the inhibition of similar CA mimics due to strong coordination of anions that block the active site.[8] This strong affinity for anion coordination also inhibits bicarbonate dissociation (Scheme 1, step 4), thereby inhibiting catalyst activity. This result suggests that the utilization of ligand environments that donate electron density into the metal center will facilitate bicarbonate dissociation and increase the rate of CO_2 hydration. Reported herein is the synthesis of small molecule enzyme mimic catalysts comprised of zinc centers with electron-donating, anionic phenanthroline ligands and analysis of CO_2 absorption under conditions conducive to industrial post-combustion carbon capture.

Results and discussion

Synthesis and characterization of zinc complexes

Salen-like ligand moieties have been extensively used as ligands for CO_2-activating catalysts.[9] These types of ligands decompose in aqueous solutions due to imine hydrolysis, making them unsuitable for aqueous amine-based post-combustion carbon capture. Therefore ligands with non-hydrolyzable imine groups serve as promising ligand scaffolds for the synthesis of more robust CO_2 hydration catalysts. The salen-like ligand 2,9-bis(2-hydroxyphenyl)-1,10-phenanthroline was explored as a scaffold for CA mimics.[10] The addition of 1.5 equiv. of zinc chloride dissolved in ethanol to a basic ethanol solution containing the yellow, acid-ligand precursor 2,9-bis(2-hydroxyphenyl)-1,10-phenanthroline resulted in the isolation of $[(Zn)_2(Phen)_2Cl(ZnCl)]$ (**1**) as a yellow powder in 94% yield (Scheme 2). The stoichiometry of the reagents has no effect on the identity of products formed; only the yield is affected. For example, using a 1 : 1 ratio of metal : ligand in the absence of pyridine still resulted in the trimetallic complex, but with a lower yield of 66%.

Slow evaporation of water/acetonitrile (H_2O/MeCN) solutions of **1** in the presence of trifuoroacetate anions resulted in the growth of yellow crystals suitable for analysis by X-ray diffraction (Fig. 1a). The single crystal X-ray structure of **1–CF_3CO_2H** shows a unique trimetallic structure. While multimetallic Zn–salen and salen-like complexes are not rare, they tend to be based on ligands designed specifically to produce multimetallic complexes through multiple metalation sites.[11] However, we are aware of no examples of similar asymmetric multi-metallic complexes. Complex **1–CF_3CO_2H** consists of two enantiomers containing two zinc-phenanthroline moieties where one (Zn(1)–Phen) contains a pseudo square pyramidal zinc bound to a phenanthroline-derived ligand in the basal position and a trifluoroacetate anion in the apical site. The other zinc–phenanthroline moiety (Zn(2)–Phen) also contains a pseudo square pyramidal zinc bound to a phenanthroline-

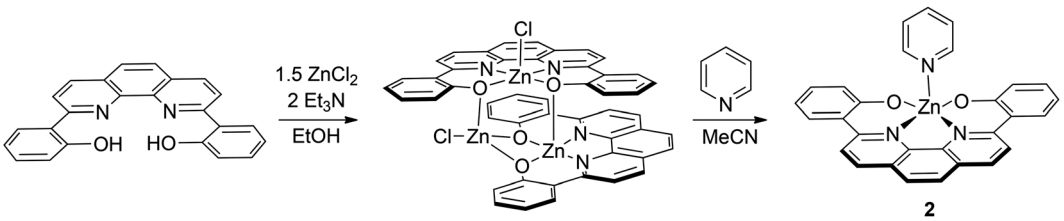

Scheme 2 Synthesis of zinc-phenanthroline complexes **1** and **2** from reaction of 2,9-bis(2-hydroxyphenyl)-1,10-phenanthroline with $ZnCl_2$ followed by reaction with pyridine.

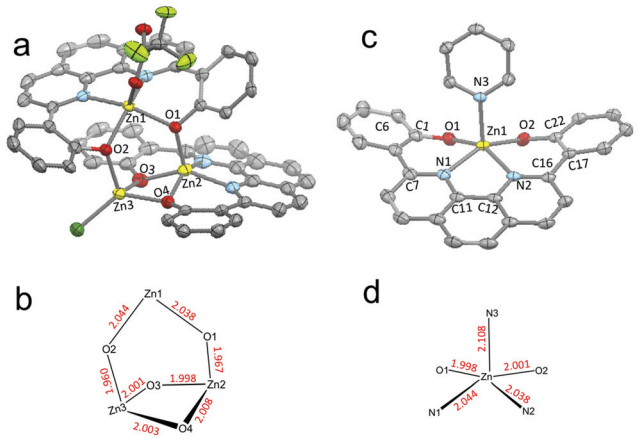

Fig. 1 (a) $[(Zn)_2(Phen)_2(CO_2CF_3)(ZnCl)]$ shown with 50% probability ellipsoids. Hydrogen atoms are omitted for clarity. (b) Schematic of selected bond lengths (Å) drawn to correspond to part a. Selected bond lengths (Å) and angles (°): Zn1–O5 1.984(3), Zn1–O1 2.038(3), Zn1–O2 2.044(3), Zn1–N2 2.095(3), Zn1–N1 2.097(3), Zn2–O2 1.960(3), Zn2–O3 2.001(3), Zn2–O4 2.003(3), Zn2–N3 2.026(4), Zn2–N4 2.045(4), Zn3–O1 1.967(3), Zn3–O3 1.998(3), Zn3–O4 2.008(3), Zn3–Cl 2.2119(12), Zn1–O1–Zn3 122.35(15), Zn2–O2–Zn1 126.01(13), Zn3–O3–Zn2 93.52(12), Zn2–O4–Zn3 93.15(13). (c) Solid-state structure of $[Zn(Phen)(C_5H_5N)]$ shown with 50% probability ellipsoids. Hydrogen atoms are omitted for clarity. Selected bond lengths (Å) and angles (°): Zn1–O1 1.9777(15), Zn1–N1 2.1052(18), Zn1–O2 1.9660(15), Zn1–N2 2.1396(17), Zn1–N3 2.1082(19), N1–C7 1.342(3), N1–C11 1.361(3), N2–C16 1.344(3), N2–C12 1.360(3), O1–C1 1.323(3), O2–C22 1.327(2), O1–Zn–O2 96.99(6), O1–Zn1–N1 86.42(7), O2–Zn1–N1 155.38(7), O2–Zn1–N2 147.59(7), N1–Zn1–N2 78.22(7), N2–Zn1–N3 109.18(7), C1–C6–C7–N1–28.1(3), N2–C16–C17–C22 19.0(3).

Table 1 Crystallographic data and structure parameters for $[(Zn)_2(Phen)_2(CO_2CF_3)(ZnCl)]$ and $[Zn(Phen)(C_5H_5N)]$

Complex	$[(Zn)_2(Phen)_2(CO_2CF_3)(ZnCl)]$	$[Zn(Phen)(C_5H_5N)]$
Empirical formula	$C_{50}H_{28}ClF_3N_4O_6Zn_3$	$C_{29}H_{19}N_3O_2Zn$
Formula weight	1069.32	506.84
T (K)	90.0(2)	90.0(2)
Wavelength	1.54178 A	0.71073
Crystal system	Monoclinic	Monoclinic
Space group	$C2/c$	$C2/c$
Unit cell dimensions		
a (Å)	30.6840(5)	16.9326(2)
b (Å)	19.1772(3)	10.5984(1)
c (Å)	19.8222(3)	25.6239(4)
α (°)	90	90
β (°)	127.333(1)	99.4547(6)
γ (°)	90	90
V (Å^3)	9274.4(3)	4535.96(10)
Z	8	8
D_{calc} (g cm^{-1})	1.532	1.484
Absorption coefficient (mm^{-1})	2.901	1.116
Crystal size (mm)	0.12 × 0.08 × 0.06	0.25 × 0.20 × 0.06
θ Range for data collection	2.93 to 68.61	1.61 to 27.51
Index ranges	$-36 \le h \le 36$	$-21 \le h \le 21$
	$-23 \le k \le 23$	$-13 \le k \le 13$
	$-23 \le l \le 23$	$-33 \le l \le 33$
Reflections collected/unique	65 553/8471	71 626/5200
Goodness-of-fit on F^2	1.079	1.042
R $[I > 2\sigma(I)]$	0.0556	0.0383
wR_2 (all data)	0.1643	0.0885

derived ligand in the basal plane, but is bridged to Zn(1)–Phen through an oxygen atom of the phenanthroline ligand in the apical site. Unexpectedly, a third tetrahedral zinc bridges the two Zn–Phen moieties. One oxygen atom from Zn(1)–Phen forms a bridging bond between the two zinc centers, whereas two oxygen atoms from Zn(2)–Phen form bridging bonds with the third zinc center. The trimetallic species is therefore based on 8-coordination bonds, forming a Zn(1)–O–Zn(2)–$(O)_2$–Zn(3)–O–Zn(1) bicyclic hexagon. Other details of data collection and structure refinement are provided in Table 1.

Formation of the trinuclear complex causes a profound difference in the Zn–O distances within each zinc center unit ranging from 1.967(3) Å to 2.044(3) Å. (Fig. 1b), which is typical of salen dimers.[12] The Zn(1)–O(1) and Zn(1)–O(2) bonds show longer distances of 2.038(3) Å and 2.044(3) Å, respectively, while Zn(3)–O(1) and Zn(2)–O(2) show shorter distances of 1.967(3) Å and 1.960(3) Å, respectively. This arrangement suggests that there is more electron donation to Zn(2) and Zn(3) compared to Zn(1). The two μ-oxos bridging Zn(2) and Zn(3) are equidistant within 3σ (2.003 ± 0.005 Å). The same trend is observed in the Zn–N distances with longer Zn(1)–N(1) and Zn(1)–N(2) at 2.096 ± 0.001 Å, and shorter Zn(2)–N(3) and Zn(2)–N(4) distances at 2.026(4) Å and 2.045(4) Å.

The trimer is based on a six-membered bicyclic ring consisting of both axially- and equatorially-coordinated oxygen atoms. We therefore reasoned that the solid-state structure may be maintained in solution. While we were unable to confirm the structure in the solution state by ^{1}H NMR spectroscopy in MeCN-d_3/pyridine-d_5 solutions,[13] analysis of the NMR solutions by electrospray ionization mass spectrometry

(ESI-MS) showed molecular ion peaks at m/z 955 and 1108, corresponding to the molecular weights of the $[(Zn)_2(Phen)_2(Zn)]^{2+}$ naked core and with two $[CD_3CN]$ fragments respectively. These results suggest that the trimeric structure is maintained in solution and in the presence of Lewis bases, such as pyridine, under ambient conditions.

To further elucidate the solution-state structure of **1**, the monomeric analog was synthesized for comparison. The monomer $[Zn(Phen)(C_5H_5N)]$ (**2**) was prepared by heating MeCN solutions of **1** in the presence of a large excess of pyridine at 80 °C for 15 h (Scheme 2). Slow cooling of a concentrated solution of **2** yielded dark yellow-brown crystals suitable for analysis by X-ray diffraction. A single crystal structure of **2** is shown is Fig. 1c. The structure contains a distorted square pyramidal zinc bound to a phenanthroline-derived ligand in the basal plane and a pyridine in the apical site. Additionally, one MeCN and one pyridine solvent molecule are contained in each asymmetric unit, but are not bound to zinc. The metal–ligand Zn–O and Zn–N bond distances are equidistant within 3σ, 1.97 ± 0.01 and 2.125 ± 0.015, respectively, which is typical of Zn^{II} complexes and suggests that the presence of pyridine prevents dimer formation.[14]

The ^1H NMR spectrum of **1** and **2** in pyridine-d_5 showed indistinguishable signals for both the phenanthroline and aryl protons. However, the solution-state structures of the two complexes were differentiated by alternative methods. Analysis of an MeCN/pyridine solution of **2** by ESI-MS and MALDI-TOF showed molecular ion peaks at m/z 427, corresponding to the molecular weight of $[Zn(Phen)]^+$. Also, **2** is soluble in MeCN while **1** requires the addition of pyridine to dissolve. These results suggest that the solution-state structure of the two complexes are different and that the trimer structure of **1** may be maintained in solution at ambient temperatures over a short time period.

Reactions with simulated flue gas

Upon identification of the potential CO_2 hydration catalysts, we embarked on testing their catalytic activities under conditions conducive to post-combustion carbon capture. Toward this goal, we utilized a rapid screening method designed as a lab-scale mimic of industrial amine-based scrubber towers to test homogeneous catalysts for CO_2 hydration under conditions conducive to industrial settings, termed delta-pH (Fig. S3†).[15] Unfortunately, neither catalyst dissolved in concentrated aqueous amine-based solvents. However, addition of MeCN as a solubilizing agent allowed for formation of homogenous solutions of **2**. While the addition of MeCN solubilizes **2** in the aqueous amine-based carbon capture solvent, it was necessary to use large amounts of pyridine to dissolve **1**, making the trimeric complex an unsuitable catalyst choice for post-combustion capture in its current state. Thus our CO_2 capture studies focus only on **2**. Passing a stream of simulated flue gas through a solution of **2** at ~0.03 mM in the carbon capture solvent (24% monoethanolamine (MEA), 20% MeCN, 56% H_2O) at ambient temperatures resulted in a more rapid drop in pH value than without **2**. This result demonstrates a more rapid rate of hydration of CO_2 when **2** is utilized and a greater absorption rate of CO_2 in the capture solution.

Analysis of the reaction mixture by UV-vis spectroscopy after exposure to CO_2 reveals that >95% of the catalyst remained intact. At a pH >10.5, the rate of CO_2 hydration is dominated by $[OH]^-$ anions. For this reason, we normalized the starting point of the delta-pH data to a value of 10.5 with an end point around pH 9.2 (Fig. 2a). This corresponds to the working range of the solvent and represents the conditions that would be observed in the absorber tower.[16] The most significant effect, observed between the pH range of 9.8 to 9.2, corresponds to the carbon-rich solution, represented at the bottom of the scrubber tower where the lowest rates of CO_2 hydration are measured.[17] A 15% increase in CO_2 absorption rate was observed compared to the baseline capture solvent without catalyst. Rate constants for **2** toward CO_2 hydration are unable to be extracted using this delta-pH method. However, in order for the catalyst to contribute to the overall CO_2 absorption rate in primary amines such as MEA, second order rate

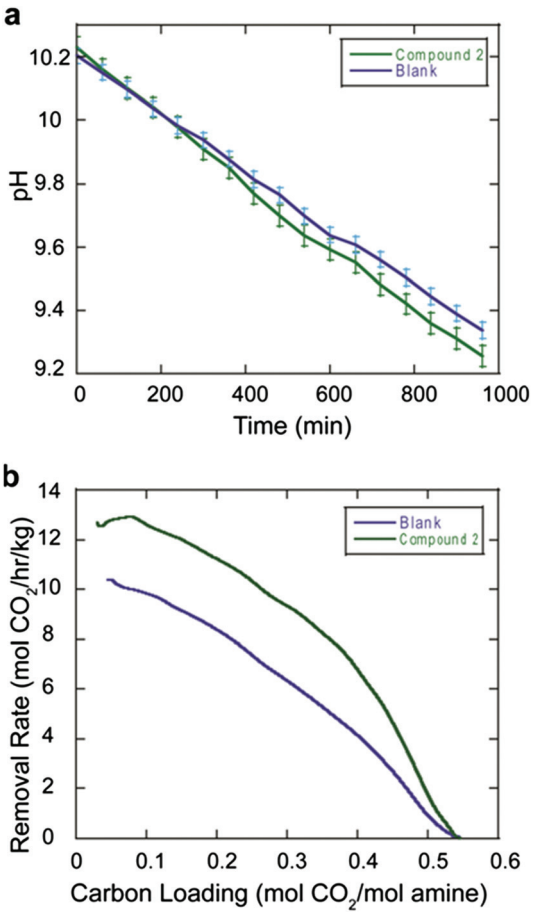

Fig. 2 (a) Delta-pH of CO_2 absorption of the capture solvent (24% MEA, 20% MeCN, 56% H_2O), "blank" (blue line) and in the presence of 0.032 mmol **2** (green line) and (b) removal rates of CO_2 absorption utilizing a breakthrough solvent evaluation apparatus of the capture solvent (24% MEA, 20% MeCN, 56% H_2O), "blank" (blue line) and in the presence of 0.032 mmol **2** (green line).

constants $>10^5$ M^{-1} s^{-1} are required (eqn (S1) and (S2)†).[18] This requirement is roughly two orders of magnitude larger than the current state-of-the-art $[Zn(cyclen)(H_2O)]^{2+}$ system.

The results of the delta-pH experiment described above are encouraging and warrant a more detailed investigation into the catalytic solvent system. Toward this goal we utilized a breakthrough solvent evaluation apparatus. Similar to the delta-pH process, a stream of simulated flue gas consisting of 14% CO_2 with N_2 span gas was bubbled through an impinger containing the solvent. The CO_2 vol% in the efflux stream was measured, and the removal rate of CO_2 determined (Fig. 2b). In the presence of **2**, an increase in removal rate of CO_2 of ~25% was observed. This enhancement was observed, and near constant, over the solvent working range of carbon loading = 0.2–0.4 mol CO_2 per mol amine.

The testing of homogeneous CO_2 hydration catalysts has only been reported in dilute tertiary amine or carbonate salt solutions in the presence of a concentrated CO_2 stream. These experiments are a far reach from conditions observed in post-combustion carbon capture, which typically utilize concentrated amine-based solvents and a dilute CO_2 stream (14%). We tentatively rationalize the capability of **2** to show enhanced CO_2 absorption in concentrated primary amines by increased electron donation into the Zn(II) metal center from the dianionic ligand, which facilitates the dissociation of bicarbonate (Scheme 1, step 4). This is believed to be the rate-limiting step and largest barrier for catalyst to overcome.[7a] Unlike the $[Zn^{II}(cyclen)(H_2O)]^{2+}$ system, which is strongly inhibited by anions like bicarbonate, the $[Zn^{II}(Phen)]$ core disfavours anion coordination due to the large electron density around the metal center. The increased electron donation into the Zn(II) center may facilitate bicarbonate dissociation but would also increase the pK_a of the aqua proton (Scheme 1, step 1). Fortunately, the pK_a is not increased to a point of inhibition from the inability to generate a needed metal hydroxo complex. This enhanced activity is also observed with structurally analogous compounds tested in our laboratory.[18]

Computational studies

As part of an effort to predict and explain the catalytic properties, behaviours, and catalysis mechanism of synthesized CA mimics under industrially-relevant conditions, density functional theory (DFT) calculations were employed at the M11/cc-pVDZ level.[19,20] Fig. 1a shows that the aromatic system connecting Zn1 to Zn2 in complex **1** are in close proximity to each other and show an interaction *via* a π-stacking, which poses a computational challenges. For the calculations, the M11/cc-pVDZ theory and basis set combination successfully reproduced the π-stacking orientation observed in the solid state structure of **1**, while the more popular basis set, LACVP, which is frequently used for transition metal complexes, failed to reproduce this π-stacking orientation. LACVP applies the LANL2DZ effective core potential only on heavy atoms and models all other atoms with the 6-31G basis set. The effective core potential lacks an accurate description of zinc; its coordination shell is poorly described and unable to reproduce the π-stacking orientation. Molecular geometry optimizations were carried out for both complexes to compare to crystal structure geometries. For both complexes, the backbones were well preserved during optimization (Table S1†), with root-mean-square deviation values of 0.328 and 0.009 for the non-H atoms between the crystal structures and optimized geometries for complexes **1** and **2**, respectively (Fig. S5†). Molecular geometries were calculated for three species thought to be involved in the catalytic process of **2**, namely Zn–OH_2, $[Zn–OH]^-$, and $[Zn–HCO_3]^-$ in order to study Zn–OH_2 deprotonation, CO_2 activation, and bicarbonate formation step as shown in Scheme 1 and compare them to CA catalysis. For these three species, the backbone geometries showed little change as a result of the optimization, but significant variation was observed in the Zn–O′ distances, with bond lengths of 2.163, 1.882, and 1.975 Å in the Zn–H_2O, $[Zn–OH]^-$, and $[Zn–HCO_3]^-$ species, respectively, which indicates variable binding strengths to the metal center (Fig. S5c†).

Kinetic studies revealed that the rate-limiting step for CA catalysis is the protolysis of water, and the same has been observed in the CA mimic zinc aza-macrocyclic catalysts (Zn–cyclens).[21] The acid dissociation constant (pK_a) is a good measure of the level of ease for Zn–OH_2 deprotonation. Our calculations of **2** revealed a pK_a of 9.3, which is higher than wild type CA (pK_a ~ 6.8) and the two reported most-active Zn-cyclen catalysts, **M2** (14 710-tetraazacyclotridecane, pK_a 8.1 [exp.]/7.6[comput.]) and **M3** (1,4,7,10-tetraazacyclododecane, pK_a 8.3[exp.]/7.6[comput.]) (Fig S6†).[21] However, this pK_a value implies that the Zn–OH_2 species of **2** is readily deprotonated in concentrated primary amine environments (pH 9.2–10.5). The increase in pK_a agrees with the Kiefer and Fierke study where the mutation of zinc bound histidine [Zn–N] to aspartic acid [Zn–O] (H119D or H94D) in CA resulted in much higher pK_a of CA zinc bound water (8.6 and 9.6, respectively).[22] Because of the basic environmental conditions of post-combustion carbon capture, the ability for **2** to deprotonate its zinc bound water is likely comparable to CA or Zn–cyclens.

To better understand the catalytic behaviour of **2**, we studied the CO_2 addition step by monitoring the (Zn–)O′···C (O_2) distance as the reaction coordinate (RC), and scanning the potential energy surface along the bond. We also calculated the structure of the transition state (TS). A nearly barrierless downhill energy curve was observed for this process. A CO_2 and $[Zn–OH]^-$ association complex was not found using restraint-free optimization, and the energy of the TS, where the RC of 2.14 Å, is approximately 0.3 kcal mol^{-1} higher than the RC of 2.20 Å, immediately before the formation of the TS (Fig. S7†). Notably, the TS is located fairly early in the RC compared to other such small-molecule catalysts, suggesting the hydroxo ligand in the $[Zn–OH]^-$ complex is a strong nucleophile.[21,23,24] The zinc-bound hydroxo moiety may destabilize a potential association complex, and result in an almost spontaneous reaction. On the other hand, the highest occupied molecular orbitals (HOMOs) of both $[Zn–OH]^-$ and $[Zn–HCO_3]^-$ (Fig. 3a) show more electron density around the O′ atom in $[Zn–OH]^-$ than the O′ in $[Zn–HCO_3]^-$, and again

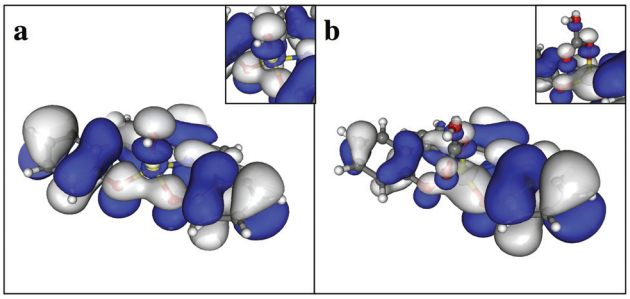

Fig. 3 HOMO of (a) Zn–OH^- and (b) Zn–HCO_3^- species and a zoom-in view of the metal center at the upper right corner. Blue and white represent positive and negative intensity values respectively.

suggest a nucleophilic zinc-bound hydroxo ligand would be reactive toward CO_2. In order to quantify the nucleophilicity of the $[Zn–OH]^-$ species of **2** to Zn–cyclen **M2** and **M3**, we performed natural population analysis (NPA). To best represent **2** under the experimental solution conditions, we used the dielectric constant of MeCN (37.5) to represent MEA (37.7), since the experimentally-measured dielectric constant for MeCN–water mixtures have been published.[25] In the gas phase, the charge of hydroxo oxygen of **2**, **M2**, and **M3** are −1.293, −1.307 and −1.298, respectively. When solvation effects are included, the hydroxo oxygen charges of **2**, **M2**, and **M3** are −1.367 when the solvent is a MeCN–water mixture. However, as shown in Table 2, row 4, when the solvent is water the hydroxo oxygen charges of **2**, **M2**, and **M3** are −1.367, −1.330, and −1.327 respectively. The greater negative charge from NPA suggests that the hydroxo ligand in **2** is more nucleophilic. In addition, the bond distance of the Zn–O(H) bond can be used to estimate the extent of the hydroxide character and compared to estimate the hydroxo nucleophilicity across different catalysts; the longer Zn–O(H) distance means a more weakly bound $[OH]^-$ and thus a stronger nucleophile.[21] Such Zn–O(H) bond distances in **2**, **M2**, and **M3** are 1.882, 1.865, and 1.849 Å, respectively (Table 2). The NPA and bond distances suggest a more nucleophilic zinc bound hydroxo ligand and should indicate an increase in the observed rate of CO_2 conversion to $[HCO_3]^-$.

Finally, we modelled different poses of the $[Zn–HCO_3]^-$ complex and computed the bond dissociation energy (BDE) for bicarbonate release (the enthalpy change associated with the bond breaking between Zn and HCO_3^-, see Computational details). Structurally, the optimized $[Zn–HCO_3]^-$ complex features the Lipscomb orientation with the –OH moiety facing up, perpendicular to the ring plane and an η^1 bicarbonate.[26] Although zinc can also adopt bidentate, η^2 coordination, the resulting distorted octahedral coordination increases the energy by ~5.5 kcal mol^{-1}, making it less favoured than the η^1 coordination structure. In fact, previous studies show that η^1 bicarbonate coordination is vital for the release of bicarbonate.[27] The HOMO of $[Zn–HCO_3]^-$ shows more electron density around the Zn(II) metal center than in $[Zn–OH]^-$ (Fig. 3b), and suggest a relatively weak coordination between Zn(II) and bicarbonate. The calculated BDE is 58.2 kcal mol^{-1}, around 3- to 5-fold smaller than the BDE of 219.2 to 251.4 kcal mol^{-1} reported for various Zn–cyclen catalysts (Table 2).[21] This difference is unsurprising given that the equilibrated Zn–O distances in $[Zn–HCO_3]^-$ are 2.163, 2.094, and 2.061 Å for **2**, **M2**, and **M3**, respectively (Table 2). A longer Zn–O distance indicates a weakly bound bicarbonate, which is more labile. The smaller BDE can also be explained by NPA. NPA on the $[Zn–HCO_3]^-$ species for the catalysts of interest, which revealed a 1.666, 1.357, and 1.360 charge for the Zn center in **2**, **M2**, and **M3** in the gas phase, and 1.645 (in water and MeCN–water mixture), 1.378, and 1.379, respectively when accounting for solvation effects (Table 2). The more positive zinc center in **2** indicates more charge donation to the metal center and lower Lewis acidity of the complexed Zn(II). The decreased Lewis acidity leads to a more weakly-bound bicarbonate and a more labile bicarbonate release.[21] Although deprotonation of $Zn–OH_2$ is the rate limiting step for CA, the release of zinc-bound bicarbonate is vital to the successful turnover of the catalytic cycle and could become the rate-limiting step when zinc-bound water is readily deprotonated in solution, as it is in Zn–cyclen and likely in **2**.[21,28] The large improvement of **2** releasing bicarbonate over Zn–cyclen may be the main cause for the observed enhanced absorption rate of CO_2.

Zn–cyclens most closely represent the zinc complex in the CA active site; however, their activities are still far below CA. Two possible reasons for the lowered activity are: (1) CA has a pocket set up for orientating CO_2 to attack the zinc bound hydroxo ligand, while Zn–cyclens have no pockets, and/or (2) the high BDEs associated with the bicarbonate release for Zn–cyclens due to a lack of a secondary coordination environment. To improve the orientation of CO_2 attack in small molecule catalysts is difficult. Extensions or "side chains" would need to be synthesized to confine the approaching CO_2, resulting in large and complex structures.[21,28] However, lowering the BDEs associated with bicarbonate release is possible. In fact, complex **2** significantly lowered bicarbonate release BDEs, *via* the change of zinc coordination from Zn-3Ns (of Zn–cyclens) to Zn- (2Ns, 2Os). Changing the chelating atoms not only enhances the reactivity of $[Zn–OH]^-$ species (compared to Zn–cyclens) but also keeps the catalytic mechanism unaltered and represents the CA catalytic cycle. In fact, this design is not far from the naturally occurring catalytic complex in CA where

Table 2 Calculated bond lengths, atomic charges and bond dissociation energy for compound **2** and Zn–cyclens, **M2** and **M3**

Parameter	2	M2	M3
Zn–O bond length (Å), $[Zn–OH]^-$	1.882	1.865	1.849
Zn–O bond length (Å), $[Zn–HCO_3]^-$	1.984	1.952	1.942
Zn–O bond length (Å), $Zn–H_2O$	2.163	2.094	2.061
O charge $[Zn–OH]^-$, solvent	−1.367	−1.330	−1.327
O charge $[Zn–OH]^-$, gas	−1.293	−1.307	−1.298
Zn charge $[Zn–HCO_3]^-$, solvent	1.645	1.378	1.379
Zn charge $[Zn–HCO_3]^-$, gas	1.666	1.357	1.360
$[Zn–HCO_3]^-$ BDE (kcal mol^{-1})	58.2	221.2	225.2

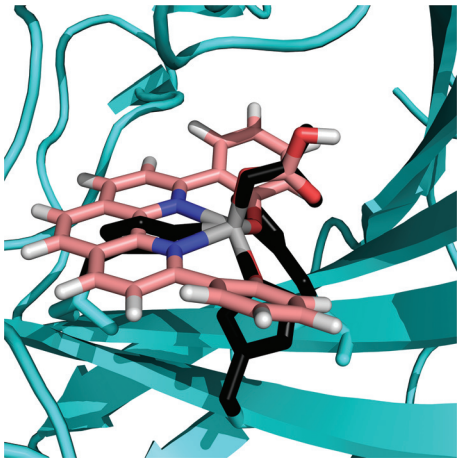

Fig. 4 The alignment of zinc complex in the human carbonic anhydrase II (carbons of zinc bound sidechains/ligands in black, Protein Data Bank ID 1XEG, see http://www.rcsb.org to access Protein Data Bank) and **2** (carbons in pink).

cobalt replaces zinc, and the enzyme adopts a Co (3Ns, 1O) (3 His and one water) to enhance bicarbonate release.[27] The superposition of **2** and CA complexed with bicarbonate (PDB 1XEG) shows an unique alignment where Zn–N(His94) and Zn–N(His119) are replaced by two Zn–O coordinations, while Zn–N(His96) lies between the two Zn–N coordinations of **2** (Fig. 4). The zinc-bound bicarbonate of CA, and **2** are all well aligned.

Conclusion

In summary, **2** exhibits a remarkable increase in CO_2 absorption rates in concentrated primary amine-based solutions from dilute fluid streams. Key to success of **2** is the use of a dianionic ligand capable of donating electron density to the Zn(II) metal center. This mediates the regeneration of the catalytically-active form by facilitating the dissociation of bicarbonate, which is typically the rate-limiting step of the reaction when under conditions conducive to carbon capture: pH values >9. The lower barrier to bicarbonate dissociation is likely the key difference leading to the high efficiency of **2**. Ongoing efforts in our laboratories are focused on increasing the solubility of derivatives of these complexes and lowering the pK_a of the aqua proton while maintaining enhanced kinetics.

Experimental details

General considerations

Routine NMR spectra were acquired on a Varian Gemini 400 MHz spectrometer (400.392 MHz for ^{1}H). All chemical shifts are reported in parts per million (ppm) relative to TMS at 0 ppm with the residual solvent peak serving as the internal reference. All mass spectra were obtained by the University of Kentucky Mass Spectrometry Facility. Matrix-assisted laser desorption/ionization time-of-flight-mass spectrometry (MALDI-TOF) spectra were obtained using a Bruker UItraflextreme operated in the Pos(+) ion mode. Electrospray ionization time-of-flight mass spectrometry (ESI-TOFMS) was obtained using an Agilent 6224 time-of-flight mass spectrometer operated in the Pos(+) ion mode of MeCN-d_3/pyridine-d_5 solutions. X-ray diffraction data was collected at 90 K on either a Nonius Kappa CCD diffractometer or a Bruker-Nonius X8 Proteum diffractometer. Crystal indexing and data processing were performed with DENZO-SMN (KappaCCD) and Bruker APEX2 (X8 Proteum). The structures were solved with SHELXS-97 and refined with SHELXL-97. Elemental analyses were performed by Atlantic Microlab, Inc., Norcross, GA. All analyses were performed in duplicate, and the reported compositions are the average of the two runs.

Methods and materials

Ethanol, toluene, diethyl ether, dichloromethane, ethyl acetate, hexane, and acetonitrile were purchased from Pharmaco-Aaper. Compressed nitrogen (ultra high purity) and carbon dioxide gases were used as received from Scott-Gross Company Inc. Antifoam (30-S) was obtained from Magrabar Chemical Corporation. Deuterated pyridine (C_5H_5N-d_5) was purchased from Cambridge Isotope Laboratories and used as received. Monoethanolamine was purchased from Univar and used as received. 2,9-Bis(2-hydroxyphenyl)-1,10-phenanthroline was prepared by literature methods.[1] All characterization data matched those referenced. All other reagents were purchased from Acros Organics or Sigma-Aldrich and used as received.

Preparation of zinc trimetallic complex [(Zn)$_2$(Phen)$_2$Cl(ZnCl)] (1). To a 100 mL round-bottomed flask was added 2,9-bis(2-hydroxyphenyl)-1,10-phenanthroline (75.0 mg, 0.206 mmol), $ZnCl_2$ (50 mg, 0.368 mmol), and EtOH (25 mL), resulting in a slurry. Triethylamine (0.06 mL, 0.45 mmol) was added slowly to the mixture. The reaction flask was immersed in a silicone oil bath at 80 °C and was stirred for 3 h followed by an ice bath for 60 min. The reaction mixture was then filtered with a Büchner funnel, and the isolated solid was washed with dichloromethane (3 × 10 mL) to give the desired product, a yellow powder (96 mg, 94%). X-ray quality crystals were grown from water/MeCN (1 : 1) solutions in the presence of sodium trifluoroacetate. MALDI-TOF (m/z): 955 [M − Cl]$^+$. Samples used for electrospray ionization mass spectrometry were from NMR samples in deuterated acetonitrile-d_3 pyridine-d_5 mixtures. ESI-MS (m/z): 1108 [M − 2Cl + 2CD$_3$CN]; 955 [M − 2Cl + H]$^+$. ^{1}H NMR (400 MHz, C_5D_5N, δ): 6.77 (td, 2H, J = 7 Hz, J = 1 Hz); 7.42 (td, 2H, J = 7 Hz, J = 1 Hz); 7.54 (dd, 2H, J = 7 Hz, J = 1 Hz); 7.77 (s, 2H); 8.04 (dd, 2H, J = 7 Hz, J = 1 Hz); 8.33 (m, 4H); ^{13}C NMR (400 MHz, C_5D_5N, δ): 172.5, 160.2, 139.8, 138.8, 133.7, 130.8, 126.4, 125.9, 125.4, 123.5, 121.1, 114.4. Samples of [(Zn)$_2$(Phen)$_2$Cl(ZnCl)] for elemental analysis contained 1 molecule of H_2O. Water is also observed in the ^{1}H NMR. The reported analysis is for [(Zn)$_2$(Phen)$_2$Cl(ZnCl)]·H_2O.

Anal. Calcd for $C_{48}H_{30}N_4O_5Cl_2Zn_3$: C, 57.09; H, 2.99; N, 5.55; Found: C, 57.19; H, 3.28; N, 5.35.

Preparation of zinc monomer complex [Zn(Phen)(C_5H_5N)] (2). To a 50 mL round-bottomed flask was added [$(Zn)_2(Phen)_2Cl(ZnCl)$] (212 mg, 0.214 mmol) dissolved in a 1 : 1 solution of MeCN : C_5H_5N (20 mL). The reaction flask was immersed in a silicone oil bath at 70 °C and was stirred for 3 h, yielding a clear, dark brown solution, which was slowly cooled to ambient temperature and stored at 8 °C for 15 h to precipitate the desired product. Filtration through a fritted funnel, then washing with hexanes (3 × 5 mL), afforded dark yellow/brown crystals of [Zn(Phen)(C_5H_5N)] (138.3 mg, 64%). ^{1}H NMR (400 MHz, C_5D_5N, δ): 6.77 (td, 2H, J = 7 Hz, J = 1 Hz); 7.42 (td, 2H, J = 7 Hz, J = 1 Hz); 7.54 (dd, 2H, J = 7 Hz, J = 1 Hz); 7.77 (s, 2H); 8.04 (dd, 2H, J = 7 Hz, J = 1 Hz); 8.33 (m, 4H). MALDI-TOF (m/z): 427 [M + H –C_5H_5N]. Samples of [Zn(Phen)(C_5H_5N)] for elemental analysis contained 0.5 equiv. of H_2O. H_2O is also observed in the ^{1}H NMR spectrum. The reported analysis is for [Zn(Phen)(C_5H_5N)]·0.5 H_2O. Anal. Calcd for $C_{26}H_{20}N_3O_{2.5}Zn$: C, 67.52; H, 3.91; N, 8.15; Found: C, 67.71; H, 4.10; N, 8.37.

CO_2 absorption studies

Representative procedure for CO_2 absorption studies: delta-pH solvent evaluation method. In a representative procedure, a carbon capture solvent stock solution was prepared (24% MEA, 20% MeCN, 56% H_2O) containing 0.01 wt% antifoam (30-S Antifoam). All subsequent solutions were made from this stock solution. To a 3-necked 250 mL round-bottomed flask was added [Zn(Phen)(C_5H_5N)] (0.032 mmol) dissolved in the MEA stock solution (25.0 mL). A pH probe was immersed in the solution through one neck, and an impinger was immersed in the solution through another neck of the flask. The solution was loaded with CO_2 by bubbling a water-saturated stream of 14 vol% CO_2 gas in N_2 supplied through a flow meter (Concoa) at 50 mL min^{-1} through the solution. Reaction progress was monitored by the change in pH over time, which decreased as CO_2 was absorbed. Controls were performed in which (1) $ZnCl_2$ was used instead of [Zn(Phen)(C_5H_5N)] and at the same molarity and (2) in which no source of zinc was incorporated into the solution (called "blank").

Breakthrough solvent evaluation method. The breakthrough solvent evaluation apparatus consists of a 30 mL gas saturator, a bubbler that contained 50 mL of solution, two condensers, and a CO_2 analyzer. Both saturator and bubbler were made of Pyrex®, and were immersed in a water bath maintained at testing temperature. A CO_2 feed gas stream balanced with N_2 was saturated with water in the saturator and bubbled through the testing solvent in the bubbler. The gas effluent was dried and analyzed for CO_2 concentration using a CO_2 analyzer (VIA-510, HORIBA, 0.5% precision). Data of CO_2 outlet concentration with respect to time was continuously recorded with 1 second interval using an in-house Labview program.

The difference of inlet and outlet CO_2 concentration represents the absorbed amount of CO_2 at a particular time. The integration of the concentration difference represents the CO_2 loading as expressed here

$$\text{CO}_2\text{ loading (mol CO}_2\text{ per kg solution)} = \frac{\int_0^t (C_{\text{in}} - C_{\text{out}}(t))\mathrm{d}t}{m_{\text{sol}}}$$

in which C_{in} is the CO_2 feed gas rate in mol s^{-1} going into the carbon capture solution, C_{out} is the CO_2 effluent rate in mol s^{-1} exiting the carbon capture solution, t is time in second, and m_{sol} is the total mass of solution in kg. The CO_2 loading refers to the total amount of CO_2 dissolved in the carbon capture solution as amine carbamate, carbonate, bicarbonate, carbonic acid, and CO_2(aq).

In addition, the absorption rate can be described by the derivate of CO_2 loading with respect to time:

$$\text{Absorption rate (mol CO}_2\text{ per kg solution per s)} = \frac{d\ \text{CO}_2\text{ loading}}{d\text{t}}$$

Computational details

The coordinates of complexes **1** and **2** from the crystal structures were used as initial starting structures for our calculations. For **2**, the crystal structure and Zn–H_2O, Zn–OH^-, and Zn–HCO_3^- species (Scheme 1) were also modelled to better understand the catalysis pathway. However, for **1** the catalysis pathway is more complicated, and thus only the geometry optimization of the crystal structure is reported here. All geometry optimization calculations were performed with the M11 functional coupled with cc-pVDZ basis set.[19,20] All calculations were carried out using GAMESS,[29] and the molecular orbitals were plotted using Molekel.[30] For geometry optimizations, only the lowest-energy conformation is included.

The bicarbonate dissociation energy is calculated as

$$E_{\text{dissociation}} = E_{\text{Zn–HCO}_3} - (E_{\text{complex}} - E_{\text{HCO}_3}),$$

where E_{complex} refers to the energy of the crystal structure with pyridine removed.

The transition state (TS) for the CO_2 addition to Zn–OH^- complex was also modelled, and the barrier was estimated using the following equation:

$$E_{\text{TS\_barrier}} = E_{\text{TS}} - E_{\text{MOH}\cdots\text{CO}_2},$$

where the second term on the right corresponds to the energy of the Zn–OH^- and CO_2 association complex, and was estimated from a series of constraint geometry optimizations that incremented CO_2 from a distance of 3.0 Å to 1.6 Å away from the hydroxo group. The pK_a was calculated using a widely used thermodynamic cycle. The detail of the procedure has been described elsewhere.[21]

Acknowledgements

We thank the University of Kentucky's Office for the Vice President for Research and the College of Arts and Sciences for start-up funding for SAO. RB thanks the University of Kentucky's Office for Undergraduate Research for a Summer

Research and Creativity Grant. YY and FCL thank Livermore Computing for the generous computer time and Dr Roger Aines and Dr Ed Lau for helpful discussions. We also thank the LLNL Grand Challenge program for the computer time. The computational portion of this work was performed under the auspices of the U.S. Department of Energy at Lawrence Livermore National Laboratory under Contract DE-AC52-07NA27344. Release number LLNL-JRNL-655987.

Notes and references

1 (*a*) *Advancing the Science of Climate Change*, National Research Council, The National Academies Press, Washington, DC, USA, 2010; (*b*) U.S. Energy Information Administration, Monthly Energy Review (November 2013).
2 Standards of Performance for Greenhouse Gas Emissions From New Stationary Sources: Electric Utility Generating Units, Environmental Protection Agency (Jan. 8, 2014).
3 Carbon Pollution - Emission Guidelines for Existing Stationary Sources: Electric Utility Generating Units, Environmental Protection Agency (June 2, 2014).
4 (*a*) U. Desideri and R. Corbelli, *Energy Convers. Manage.*, 1998, **39**, 857–867; (*b*) P. Riemer, H. Audus and A. Smith, *Carbon Dioxide Capture from Power Stations*, IEA Greenhouse Gas R&D Programme, Cheltenham, United Kingdom, 1993; (*c*) C. Hendriks, *Carbon Dioxide Removal from Coal-fired Power Plants*, Kluwer Academic Publishers, The Netherlands, 1994, pp. 14–223.
5 (*a*) K. M. Merz, M. A. Murcko and P. A. Kollman, *J. Am. Chem. Soc.*, 1989, **111**, 5636–5649; (*b*) V. M. Krishnamurthy, G. K. Kaufman, A. R. Urbach, I. Gitlin, K. L. Gudiksen, D. B. Weibel and G. M. Whitsides, *Chem. Rev.*, 2008, **108**, 946–1051; (*c*) A. E. Eriksson, T. A. Jones and A. Liljas, *Proteins*, 1988, **4**, 274–282.
6 D. Matulis, J. K. Kranz, F. R. Salemme and M. J. Todd, *Biochemistry*, 2005, **44**, 5258–5266.
7 (*a*) X. Zhang, R. van Eldik, T. Koike and E. Kimura, *Inorg. Chem.*, 1993, **32**, 5749–5755; (*b*) X. Zhang and R. Van Eldik, *Inorg. Chem.*, 1995, **34**, 5606–5614; (*c*) R. Davy, *Energy Procedia*, 2009, **1**, 885–892; (*d*) N. L. Zastrow, A. F. A. Peacock, J. A. Stuckey and V. L. Pecoraro, *J. Inorg. Biochem.*, 2002, **89**, 255–266; (*e*) D. Huang, O. V. Makhlynets, L. T. Tan, S. C. Lee, E. V. Rybak-Akimova and R. H. Holm, *Proc. Natl. Acad. Sci. U. S. A.*, 2011, **108**(4), 1222–1227; (*f*) D. Huang, O. V. Makhlynets, L. T. Tan, S. C. Lee, E. V. Rybak-Akimova and R. H. Holm, *Inorg. Chem.*, 2011, **50**(20), 10070–10081; (*g*) G. Parkin, *Chem Rev.*, 2004, **104**(2), 699–767.
8 Unpublished work by C. A. Lippert, D. Gupta, A. Wishrojwar, J. P. Selegue, J. E. Remias and K. Liu.
9 (*a*) R. L. Paddock and S. T. Nguyen, *Chem. Commun.*, 2004, 1622–1623; (*b*) D. J. Darensbourg, Personal Adventures in the Synthesis of Copolymers from Carbon Dioxide and Cyclic Ethers, in *Contribution in Advances in Inorganic Chemistry Volume 66: CO_2 Chemistry*, ed. R. van Eldik and M. Aresta, Elselvier Inc., Burlington, Academic Press, 2014, pp. 1–23; (*c*) D. J. Darensbourg, W.-W. Chung and S. J. Wilson, *ACS Catal.*, 2013, **3**, 3050–3057; (*d*) D. J. Darensbourg and G.-P. Wu, *Angew. Chem., Int. Ed.*, 2013, **52**, 10602–10606; (*e*) W. Clegg, R. W. Harrington, M. North and R. Pasquale, *Chem. – Eur. J.*, 2010, **16**, 6828–6843; (*f*) M. North and R. Pasquale, *Angew. Chem., Int. Ed.*, 2009, **48**(16), 2946–2948.
10 (*a*) S.-N. Pun, W. H. Chung, K.-M. Lam, P. Guo, P. H. Chan, K.-Y. Wong, C.-H. Che, T.-Y. Chen and S.-M. Peng, *J. Chem. Soc., Dalton Trans.*, 2002, 575–583; (*b*) A. Orejón, A. Castellanos, P. Salagre, S. Castillón and C. Claver, *Can. J. Chem.*, 2005, **83**, 764–768.
11 (*a*) Z. Wang, W. Feng, P. Su, Z. Zhang, Y. Zhang, T. Miao, Z. Lü, D. Fang, W.-K. Wong and R. A. Jones, *Inorg. Chem. Commun.*, 2013, **36**, 11–13; (*b*) K.-L. Kuo, C.-C. Huang and Y.-C. Lin, *Dalton Trans.*, 2008, 3889–3898; (*c*) M. M. Belmonte, E. C. Escuedero-Adán, E. Martin and A. W. Kleij, *Dalton Trans.*, 2012, **41**, 5193–5200; (*d*) Y. Zhang, W. Feng, H. Liu, Z. Zhang, X. Lü, J. Song, D. Fan, W.-K. Wong and R. A. Jones, *Dalton Trans.*, 2012, **24**, 148–152; (*e*) T. Nabeshima and M. Yamamura, *Pure Appl. Chem.*, 2013, **85**(4), 763–776; (*f*) R. M. Haak, A. M. Castilla, M. M. Belmonte, E. C. Escuedero-Adán, J. Benet-Bucholz and A. W. Kleij, *Dalton Trans.*, 2011, **40**, 3352–364; (*g*) H. Liu, Y. Zhang, W.-X. Feng, P.-Y. Su, G.-X. Shi, Z. Zhang, D.-D. Fan, R. Lu, Z.-Q. Lü, W.-K. Wong and R. A. Jones, *Inorg. Chem. Commun.*, 2013, **35**, 213–216.
12 (*a*) G. Consiglio, S. Failla, P. Finocchiaro, I. P. Oliveri and S. DiBella, *Inorg. Chem.*, 2012, **51**, 8409–8418; (*b*) K. G. Vladimirova, A. Y. Freidzon, O. V. Kotova, A. A. Vaschenko, L. S. Lepnev, A. A. Bagatur'yants, A. G. Vitukhnovskiy, N. F. Stepanov and M. V. Alfimov, *Inorg. Chem.*, 2009, **48**, 11123–11130.
13 NMR of both species are identical due to symmetry of the complexes.
14 A. W. Kleij, M. Kuil, M. Lutz, D. M. Tooke, A. L. Spek, C. J. Kamer, W. N. M. van Leeuwen and J. N. H. Reek, *Inorg. Chim. Acta*, 2006, **359**, 1807–1814.
15 G. M. Bond, J. Stringer, D. K. Brandvold, F. A. Simsek, M.-G. Medina and G. Egeland, *Energy Fuel*, 2001, **15**, 309–316.
16 R. A. Frimpong, D. Johnson, L. Richburg, B. Hogston, J. E. Remias, J. K. Neathery and K. Liu, *Chem. Eng. Res. Des.*, 2013, **91**, 963–969.
17 Cost and Performance Baseline for Fossil Energy Plants" DOE/NETL-2007/1281, Volume 1: Bituminous Coal and Natural Gas to Electricity, Final Report (Original Issue Date, May 2007) Revision 1, August 2007.
18 C. A. Lippert, K. Liu, M. Sarma, S. R. Parkin, J. E. Remias, C. M. Brandewie, S. A. Odom and K. Liu, *Catal. Sci. Technol.*, 2014, **4**, 3620–3625.
19 R. Peverati and D. G. Truhlar, *J. Phys. Chem. Lett.*, 2012, **3**, 117–124.
20 T. H. Dunning Jr., *J. Chem. Phys.*, 1989, **90**, 1007–1023.

21 L. Koziol, C. A. Valdez, S. E. Baker, E. Y. Lau, W. C. Floyd III, S. E. Wong, J. H. Satcher Jr., F. C. Lightstone and R. D. Aines, *Inorg. Chem.*, 2012, **51**, 6803–6812.
22 L. L. Kiefer and C. A. Fierke, *Biochemistry*, 1994, **33**, 15233–15240.
23 S. E. Wong, E. Y. Lau, H. J. Kulik, J. H. Satcher, C. Valdez, M. Worsely, F. C. Lightstone and R. D. Aines, *Energy Procedia*, 2011, **4**, 817–823.
24 S. S. Glad and F. Jensen, *J. Chem. Soc., Perkin Trans. 2*, 1994, 871–876.
25 L. G. Gagliardi, C. B. Castells, C. Rafols, M. Roses and E. Bosch, *J. Chem. Eng. Data*, 2007, **52**(3), 1103–1107.
26 J. Y. Liang and W. N. Lipscomb, *Biochemistry*, 1987, **26**(17), 5293–5301.
27 E. Y. Lau, S. E. Wong, S. E. Baker, J. P. Bearinger, L. Koziol, C. A. Valdez, J. H. Satcher Jr., R. D. Aines and F. C. Lightstone, *PLoS One*, 2013, **8**, e66187.
28 L. Koziol, S. G. Essiz, S. E. Wong, E. Y. Lau, C. A. Valdez, J. H. Satcher Jr., R. D. Aines and F. C. Lightstone, *J. Chem. Theory Comput.*, 2013, **9**, 1320–1327.
29 M. W. Schmidt, K. K. Baldridge, J. A. Boatz, S. T. Elbert, M. S. Gordon, J. H. Jensen, S. Koseki, N. Matsunaga, K. A. Nguyen, S. Su, T. L. Windus, M. Dupuis and J. A. Montgomery, *J. Comput. Chem.*, 1993, **14**, 1347–1363.
30 *MOLEKEL, 5.4.0.8*, Swiss National Supercomputing Centre, Lugano, Switzerland, http://molekel.cscs.ch/wiki/pmwiki.php.